Paper published in: Int. J. Rock Mech. Min. Sci., vol. 99, pp. 9-20, 2017

Finite Element Simulations of Interactions between Multiple Hydraulic Fractures in a Poroelastic Rock

Saeed Salimzadeh[1,2], Tomoya Usui[1], Adriana Paluszny[1], and Robert W. Zimmerman[1]

[1]Department of Earth Science and Engineering, Imperial College, London, UK

[2]Centre for Oil and Gas, Technical University of Denmark, Lyngby, Denmark

ABSTRACT

A fully coupled three-dimensional finite-element model for hydraulic fracturing in permeable rocks is utilised to investigate the interaction between multiple simultaneous and sequential hydraulic fractures. Fractures are modelled as surface discontinuities within a three-dimensional matrix. This model simultaneously accounts for laminar flow within the fracture, Darcy flow within the rock matrix, poroelastic deformation of the rock, and the propagation of fractures using a linear elastic fracture mechanics framework. The leakoff of fracturing fluid into the surrounding rocks is defined as a function of the pressure gradient at the fracture surface, the fluid viscosity, and the matrix permeability. The coupled equations are solved numerically using the finite element method. Quadratic tetrahedral and triangle elements are used for spatial discretisation of volumes and surfaces, respectively. The model is validated against various analytical solutions for plane-strain and penny-shaped hydraulic fractures. Several cases of simultaneous fracturing of multiple hydraulic fractures are simulated in which the effects of the various parameters (the *in situ* stresses, the distance between fractures, the permeability of the matrix, the Biot poroelastic coefficient, and the number of the fractures in a group) are investigated. The results show that the stress induced by the opening of the fractures, and the stress induced by the fluid leakoff, each have the effect of locally altering the magnitudes and orientations of the principal stresses, hence altering the propagation direction of the fractures. Opening of a fracture induces excessive compression (also known as the "stress shadow") that causes adjacent fractures to curve away from each other. This excessive compression competes against the differential *in situ* stresses, which tend to cause the fracture to grow in the plane normal to the minimum *in situ* stress. The stress shadow effect is reduced by increasing the distance between fractures, or by increasing the leakoff, which may be due to increased permeability of the rock, or an increase in the Biot coefficient.

Keywords: Multiple hydraulic fractures; sequential fracturing; simultaneous fracturing; linear elastic fracture mechanics

1. Introduction

Hydraulic fracturing can greatly enhance well productivity in unconventional reservoirs. Consequently, most drilled horizontal wells are hydraulically fractured [1,2]. In practice, hydraulic fracturing of horizontal wells occurs in several stages, from the "toe" towards the "heel" of the well. At each fracturing stage, a number of perforation clusters are created over a section of the well, and simultaneously pressurised. Each perforation cluster serves as the initiation point of a hydraulic fracture [3]. The stress field in the surrounding rocks is altered during the hydraulic fracturing process, and additional compression is developed due to the fracture opening, and the poroelastic deformation of the rock. This compression affects the fracture creation in the nearby rock, known as "stress shadowing" in the hydraulic fracturing literature. Despite improvements in diagnostic technology, such as micro-seismic monitoring, modelling of hydraulic fracturing is an important tool that allows engineers to design and estimate the fracture geometry, since it is still difficult to measure the actual fracture geometry directly. Robust numerical models that simultaneously account for fluid flow through fractures and matrix, fracture propagation, and rock deformation, are required for accurate simulation of interacting fractures.

Although a variety of analytical and numerical solutions have been developed for a single hydraulic fracture [2], few studies have been done on multiple hydraulic fractures, and the interaction between hydraulic fractures and natural fractures. Different numerical approaches have been used for modelling single hydraulic fractures, including the boundary integral method [4], the distinct element method [5], the finite element method (2D: [6]; 3D: [7,8]), discrete fracture network [9], the embedded fracture model [10], the lattice approach [11], the phase-field model [12], and the extended finite element method [13-15]. Fluid flow through the fracture is commonly modelled using lubrication theory, which is derived from the general Navier-Stokes equation for flow of a fluid between two parallel plates [16,17], whereas the fracture aperture is calculated using linear elasticity [18,19].

In the case of multiple hydraulic fractures driven from a single horizontal well, compression due to the nearby fractures tends to close the fracture. This effect is known as the "stress shadow effect" [20]. The stress shadow effect causes fractures to deviate from the initial plane normal to the minimum *in situ* stress. Olson and Dahi-Taleghani [21] investigated the interaction between the hydraulic and natural fractures using a 2D numerical model. Cheng [22] investigated the effect of hydraulic fracture spacing on

fracture interactions using a 2D boundary element method. Several studies have been proposed for 2D or pseudo-3D models for the problem of multiple hydraulic fractures interaction [23-28]. Among 3D models, Peirce and Bunger [29] proposed solutions for multiple fractures with simplified interactions. Kumar and Ghassemi [30] proposed a 3D numerical model using the Displacement Discontinuity method, in which fluid flow through fractures is coupled sequentially to the elastic deformation of the reservoir [31]. Sequential coupling, in a highly non-linear system such as in hydraulic fracturing, suffers convergence problems, and requires manual interference to converge. Furthermore, the effect of poroelasticity has been either neglected by ignoring the leakoff, or simplified by assigning a sink term into the flow equation in the fracture in order to account for leakoff [32]. In fact, poroelastic effects may have a significant influence on hydraulic fracturing variables such as injection pressure, fracture aperture, fracture length, and interactions [7, 33].

In the present study, a robust three-dimensional, fully coupled, finite element model for multiple hydraulic fracturing is presented. The model accounts for laminar flow within the fracture, Darcy flow within the rock matrix, the propagation of the fracture, and poroelastic deformation of the rock. The three governing equations are solved simultaneously. The onset and direction of fracture growth are estimated using three modal stress intensity factors computed along the fracture tip [34]. The displacement correlation method is used for computing the modal stress intensity factors [35]. The model is validated against various analytical solutions for different regimes of propagation [36], and subsequently applied to study the interaction between multiple hydraulic fractures. The accuracy of the proposed model is evident from the validation examples presented in this work. The effects of poroelasticity and differential *in situ* stress (the difference between the minimum *in situ* stress and the other two *in situ* stresses) on the interaction between fractures are investigated. Both simultaneous and sequential fracturing of multiple fractures are simulated.

2. Computational Model

Fractures are represented discretely using two-dimensional surfaces within a three-dimensional domain. When deriving the governing equations, each fracture is represented by a discontinuity Γ_c in the domain Ω with boundary Γ, as shown in Fig. 1. Fluid flow through the fractures is modelled based on lubrication theory. Assuming a piecewise

planar fracture, in which the lateral extent of the fracture surface is much larger than the fracture aperture, the average velocity of fluid along the fracture plane may be calculated using the cubic law as [37]

$$\mathbf{v}_f = -\frac{{a_f}^2}{12\mu_f}\nabla p_f \tag{1}$$

where a_f is the fracture aperture, μ_f is the fluid viscosity, and p_f is the fracture fluid pressure. The fracture aperture is given by the differential displacement between two sides of the fracture, $a_f = (\mathbf{u}^+ - \mathbf{u}^-).\mathbf{n}_c$, where $\mathbf{u}^+$ and $\mathbf{u}^-$ are the displacements of the two opposing faces of the fracture, and $\mathbf{n}_C$ is the outward unit normal to the fracture surface [7,14]. The fluid within the fracture applies hydraulic loading on the fracture surfaces as

$$\mathbf{T}_c = -p_f\mathbf{n}_C \tag{2}$$

The shear tractions exerted by the fracturing fluid on the fracture walls is assumed to be negligible. The variation in the fracture aperture is a consequence of the mechanical deformation of the rock matrix under the combined effects of pressure and stress perturbations. The mechanical deformation model is based on the condition of stress equilibrium for a representative elementary volume of the porous medium, saturated with a single fluid. The stress-strain relationship of the element is expressed as

$$\boldsymbol{\sigma}' = \mathbf{D}\boldsymbol{\varepsilon} \tag{3}$$

where $\boldsymbol{\sigma}'$ is the effective stress, $\mathbf{D}$ is the drained stiffness matrix, and $\boldsymbol{\varepsilon}$ is the strain tensor in the porous medium. The effective stress is defined exclusively within the rock matrix, linking the change in stress to the change in strain. The effective stress for a rock matrix saturated with a single-phase fluid is defined as [38]

$$\boldsymbol{\sigma}' = \boldsymbol{\sigma} + \alpha p_m\mathbf{I} \tag{4}$$

where $\boldsymbol{\sigma}$ is the total stress, α is the Biot coefficient, p_m is the fluid pressure in the matrix, and $\mathbf{I}$ is the second-order identity tensor. The Biot coefficient is defined as

$$\alpha = 1 - K/K_s \tag{5}$$

where K and K_S are the bulk moduli of the porous rock and of the rock matrix material (*e.g.* mineral grains), respectively [39]. The fully coupled governing equations for mechanical deformation, fracture flow, and matrix flow can be written respectively as [7]

$$\int_\Omega[\mathrm{div}(\mathbf{D}\boldsymbol{\varepsilon} - \alpha p_m\mathbf{I}) + \mathbf{F}]d\Omega - \int_{\Gamma_c} p_f\mathbf{n}_c d\Gamma = 0 \tag{6}$$

$$\operatorname{div}\left(\frac{{a_f}^3}{12\mu_f}\nabla p_f\right) = a_f c_f \frac{\partial p_f}{\partial t} + \frac{\partial a_f}{\partial t} - \frac{k_n}{\mu_f}\frac{\partial p}{\partial n_c} \quad (7)$$

$$\int_\Omega \operatorname{div}\left[\frac{\mathbf{k}_m}{\mu_f}(\nabla p_m + \rho\mathbf{g})\right] d\Omega = \int_\Omega \left[\alpha\frac{\partial(\operatorname{div} u)}{\partial t} + \left(\phi c_f + \frac{\alpha-\phi}{K_s}\right)\frac{\partial p_m}{\partial t}\right] d\Omega + \int_{\Gamma_c}\frac{k_n}{\mu_f}\frac{\partial p}{\partial n_c}\, d\Gamma \quad (8)$$

in which $\boldsymbol{\varepsilon} = \frac{1}{2}(\nabla\mathbf{u} + \nabla\mathbf{u}^T)$ is the strain tensor in the porous medium, $\mathbf{u}$ is the displacement vector, $\mathbf{F}$ is the body force per unit volume, $\mathbf{n}_c$ is the unit normal to the fracture, c_f is the fluid compressibility, $\mathbf{k}_m$ is the permeability tensor of the rock matrix, k_n is the permeability of the rock matrix in the direction normal to the fracture, $\frac{\partial p}{\partial n_c}$ is the gradient of the pressure perpendicular to the fracture, ρ is the fluid density, $\mathbf{g}$ is the vector of gravitational acceleration, and ϕ is the rock matrix porosity. The last term in equations (7) and (8) represents the fluid exchange between fracture and matrix (leakoff). Leakoff is defined in terms of the matrix permeability in the direction normal to the fracture (k_n), the fluid viscosity, and the pressure gradient at the fracture wall. The above-mentioned governing equations have the following properties:

(a) Setting $\alpha = 0$ will decouple the mechanical deformation model and the matrix flow model, in which case mechanical loading will have no direct effect on the matrix pressures, and vice versa.

(b) In contrast to the above situation, fracture pressures will always be coupled to the mechanical deformation model, irrespective of the value of the Biot coefficient.

(c) Equation (7) reduces to the lubrication equation [16] for the case of one-dimensional incompressible flow with no leakoff.

(d) The time-derivative of the fracture aperture, $\partial a_f/\partial t$, in eq. (7) provides direct coupling between the displacement field and the fracture flow field, which is symmetric to the fracture pressure loading term, $p_f\mathbf{n}_C$, in eq. (6).

3. Finite Element Approximation

The finite element method has been utilised to spatially discretise the governing equations. Three displacement components ($\mathbf{u}$), and fluid pressures in the fracture (p_f) and matrix (p_m) are defined as primary variables. Using the standard Galerkin method, the displacements and pressures within an element are approximated from their nodal values. A finite difference technique is employed to march the solution forward in time. The final form of the discretised equations are described in the form of $\mathbb{S}\mathbb{X} = \mathbb{F}$ as [7]

$$\begin{bmatrix} -\mathbf{K} & \mathbf{C}_m & \mathbf{C}_f \\ \mathbf{C}_m^T & \mathbf{H}_m dt + \mathbf{M}_m + \mathbf{L}dt & -\mathbf{L}dt \\ \mathbf{C}_f^T & -\mathbf{L}dt & \mathbf{H}_f dt + \mathbf{M}_f + \mathbf{L}dt \end{bmatrix} \begin{Bmatrix} \widehat{\mathbf{u}}^{t+\Delta t} \\ \widehat{\mathbf{p}}_m{}^{t+\Delta t} \\ \widehat{\mathbf{p}}_f{}^{t+\Delta t} \end{Bmatrix} = \begin{Bmatrix} -\mathbf{F} \\ \mathbf{C}_m^T \widehat{\mathbf{u}}^t + \mathbf{M}_m \widehat{\mathbf{p}}_m{}^t + \mathbf{Q}_m dt \\ \mathbf{C}_f^T \widehat{\mathbf{u}}^t + \mathbf{M}_f \widehat{\mathbf{p}}_f{}^t + \mathbf{Q}_f dt \end{Bmatrix} \quad (9)$$

where

$$\mathbf{K} = \int_\Omega \mathbf{B}_1{}^{\mathrm{T}} \mathbf{D} \mathbf{B}_1 d\Omega \quad (10)$$

$$\mathbf{C}_m = \int_\Omega \mathbf{B}_2{}^{\mathrm{T}} \alpha \mathbf{N} d\Omega \quad (11)$$

$$\mathbf{C}_f = \int_{\Gamma_c} \mathbf{N}^{\mathrm{T}} \mathbf{n}_c \mathbf{N}_{\boldsymbol{c}} d\Gamma \quad (12)$$

$$\mathbf{H}_m = \int_\Omega \mathbf{B}_3{}^{\mathrm{T}} \frac{\mathbf{k}_m}{\mu} \mathbf{B}_3 d\Omega \quad (13)$$

$$\mathbf{H}_f = \int_{\Gamma_c} \nabla \mathbf{N}_{\boldsymbol{c}}{}^{\mathrm{T}} \frac{{a_f}^3}{12\mu_f} \nabla \mathbf{N}_{\boldsymbol{c}} d\Gamma \quad (14)$$

$$\mathbf{M}_m = \int_\Omega \mathbf{N}^{\mathrm{T}} \left(\phi c_f + \frac{\alpha - \phi}{K_s} \right) \mathbf{N} d\Omega \quad (15)$$

$$\mathbf{M}_f = \int_{\Gamma_c} \mathbf{N}_{\boldsymbol{c}}{}^{\mathrm{T}} a_f c_f \mathbf{N}_{\boldsymbol{c}} d\Gamma \quad (16)$$

$$\mathbf{L} = \int_{\Gamma_c} \mathbf{N}_{\boldsymbol{c}}{}^{\mathrm{T}} \frac{k_m}{\mu_f} \frac{\partial \mathbf{N}_c}{\partial \mathbf{n}_c} d\Gamma \quad (17)$$

where $\mathbf{K}$ is the mechanical stiffness matrix, $\mathbf{C}_f$ and $\mathbf{C}_m$ are the hydro-mechanical and poroelastic coupling matrices, respectively, $\mathbf{H}$ is the conductance matrix, $\mathbf{M}$ is the capacitance mass matrix, $\mathbf{L}$ is the leakoff mass matrix, $\mathbf{F}$ is the applied load vector, $\mathbf{Q}$ is the fluid flux, and $\widehat{\mathbf{u}}$ and $\widehat{\mathbf{p}}$ are the vectors of nodal values of displacement and fluid pressure, respectively. The matrices $[\mathbf{B}_1]_{6\times 3n} = \overline{\nabla}\mathbf{N}$, $[\mathbf{B}_2]_{1\times 3n} = \boldsymbol{\delta}^{\mathbf{T}}\mathbf{B}_1$, and, $[\mathbf{B}_3]_{3\times n} = \nabla\mathbf{N}$ are derivatives of the shape function, $\boldsymbol{\delta} = \{1 \quad 1 \quad 1 \quad 0 \quad 0 \quad 0\}^T$, and ∇ is the gradient operator. Superscript t represents the time at the current step, superscript $t + dt$ represents time at the next step, and dt is the time increment. The non-diagonal components of the stiffness matrix are populated with the coupling matrices $\mathbf{C}_f$ for hydro-mechanical coupling in the fracture, $\mathbf{C}_p$ for poroelastic coupling in the matrix, and $\mathbf{L}$ for fracture-matrix flow coupling. The operator $\overline{\nabla}$ for three-dimensional displacement field is defined as

$$\overline{\nabla} = \begin{bmatrix} \frac{\partial}{\partial x} & 0 & 0 \\ 0 & \frac{\partial}{\partial y} & 0 \\ 0 & 0 & \frac{\partial}{\partial z} \\ 0 & \frac{\partial}{\partial z} & \frac{\partial}{\partial y} \\ \frac{\partial}{\partial z} & 0 & \frac{\partial}{\partial x} \\ \frac{\partial}{\partial y} & \frac{\partial}{\partial x} & 0 \end{bmatrix} \quad (18)$$

Two types of discretisation are used: quadratic tetrahedra for volume elements, and quadratic triangles for surface elements (fractures). The triangles on two opposite surfaces of a fracture are matched with each other, but they don't share nodes, and duplicate nodes are defined for two sides of a fracture (except for the nodes on fracture tip). The triangles are matched with faces of the tetrahedral connected to the fracture, and therefore share the same nodes. However, the model presented in this study can also be applied to non-matching elements. The fracture flow equation (Eq. 2) is solved only on one-side of the fracture (*i.e.*, matrices $\mathbf{H}_f$ and $\mathbf{M}_f$ are accumulated over triangle elements on one side of the fracture), whereas the coupling matrices ($\mathbf{C}_f$ and $\mathbf{L}$) are accumulated on both sides of the fracture. Mechanical deformation and matrix flow equations are accumulated over the tetrahedral elements. As the components of the stiffness matrix $\mathbb{S}$ are dependent on the primary unknown variables $\mathbb{X}$, a Picard iteration procedure is adopted to reach the correct solution within acceptable tolerance. For the current iteration $s+1$ in current step $n+1$, the solution-dependant coefficient matrices in the stiffness matrix are updated using weighted average solution vector $\mathbb{X}_{n+1}^{s+\theta}$ defined as

$$\mathbb{X}_{n+1}^{s+\theta} = (1-\theta)\mathbb{X}_{n+1}^{s-1} + \theta\mathbb{X}_{n+1}^{s} \tag{19}$$

where $\mathbb{X}_{n+1}^{s-1}$ and $\mathbb{X}_{n+1}^{s}$ are the solution vectors of two most recent iterations in the current timestep $n+1$, and $\theta = 2/3$ is the weighing coefficient. For the first iteration $s = 1$, the previous timestep solution is used as

$$\mathbb{X}_{n+1}^{0} = \mathbb{X}_{n+1}^{1} = \mathbb{X}_{n} \tag{20}$$

where $\mathbb{X}_n$ is the solution vector from timestep n. The iterations are repeated, until consecutive values of $\mathbb{X}_{n+1}^{s}$ agree to within a specified tolerance ε

$$\frac{\|\mathbb{X}_{n+1}^{s+1} - \mathbb{X}_{n+1}^{s}\|}{\|\mathbb{X}_{n+1}^{s+1}\|} < \varepsilon \tag{21}$$

The discretised coupled equations are implemented as part of the Imperial College Geomechanics toolkit [40], which interacts with an octree volumetric mesher (ANSYS ICEM) and the Complex Systems Modelling Platform (CSMP++, also known as CSP), an object-oriented application programme interface (API), for the simulation of complex geological processes and their interactions (formerly CSP, *cf.* [41]). The set of linear algebraic equations are solved with the algebraic multigrid method for systems, SAMG [42].

4. Stress Intensity Factors and Growth Model

The mechanical deformation of the rock leads to concentrations of stress around the fracture tips, which can be quantified locally at each tip by the stress intensity factors (SIFs). The SIFs are key parameters in evaluating and predicting the onset of fracture growth, and the growth direction. In this study, three stress intensity factors (SIFs) for three modes of fracture opening are computed using the displacement correlation (DC) method. The DC method is computationally very cheap and is able to yield very good approximations to the SIFs [35]. The three SIFs are mode I (K_I) for opening due to tensile loading, mode II (K_{II}) for in-plane shearing due to sliding, and mode III (K_{III}) for out-of-plane shearing due to tearing. The crack grows if and when the equivalent stress intensity factor K_{eq} overcomes the material toughness (k_{ic}). The equivalent SIF in the direction of propagation (θ_p) is calculated as [43]

$$K_{eq} = \frac{1}{2}\cos\left(\frac{\theta_p}{2}\right)\left\{K_{cs} + \sqrt{K_{cs}^2 + 4K_{III}^2}\right\} \tag{22}$$

where $K_{cs} = K_I \cos^2\left(\frac{\theta_p}{2}\right) - \frac{3}{2}K_{II}\sin(\theta_p)$, and θ_p is the propagation angle. The in-plane propagation angle (θ_p) and out-of-plane deflection angle (ψ_p) are determined using a modified maximum circumferential stress method that takes into account modal stress intensity factors under mixed loading [43]. The in-plane propagation angle (θ_p) is assumed to be perpendicular to the maximum circumferential stress σ_1, thus, θ_p can be calculated by

$$\frac{\partial \sigma_1}{\partial \theta} = 0, \qquad \text{and} \qquad \frac{\partial^2 \sigma_1}{\partial \theta^2} < 0 \tag{23}$$

The out-of-plane deflection angle ψ_p is defined by the orientation of σ_1 as

$$\psi_p = \frac{1}{2}\tan^{-1}\left(\frac{2\tau_{\theta z}}{\sigma_\theta - \sigma_z}\right) \tag{24}$$

The SIFs and growth computations are performed at fifty locations along the fracture tip.

5. Model Validation

The finite element code has been previously validated against various analytical solutions [7] and experimental data [33]. In this section, two examples of model validation are presented: the simulation of plane-strain and penny-shaped hydraulic fractures under *viscosity* and *toughness* propagation regimes. Analytical solutions for these two geometries are available in the literature for both the viscosity-dominated and toughness-dominated regimes.

5.1. Plane-strain (KGD) hydraulic fracture

A plane-strain hydraulic fracture is modelled in this section to test the accuracy of the proposed computational approach. The plane-strain assumption is suitable for short fractures, i.e., when the fracture length is much smaller than its height. This fracture is also known as a KGD fracture, as the analytical solution for hydraulic fracturing variables of pressure, aperture and fracture length was first proposed by Khristianovic and Zheltov [44], and Geertsma and de Klerk [18]. In this simulation, a viscous fluid with viscosity $\mu = 0.1$ Pa s, is injected into a fracture with initial half-length of 1 m and height of 20 m. The injection rate is set to $q = 1$ m^3/min. The host formation has a Young's modulus of $E = 1$ MPa, and a Poisson's ratio of $\nu = 0.3$. Fracture toughness is set to K_{ic} = 1×10^6 Pa m$^{0.5}$. This set of parameters corresponds to the viscosity-dominated regime [36]. Due to the symmetry of the problem, only half of the fracture geometry is modelled, as shown in Fig. 2. The spatial discretisation, and the results for injection pressure, fracture width (aperture), and fracture length, are shown in Fig. 2. Injection pressure decreases as the hydraulic fracture grows, while the fracture aperture increases with time. Included in this figure is the analytical solution by Geertsma and de Klerk [18]. Very good agreement is found between the present model and the analytical solutions.

5.2. Penny-shaped (radial) hydraulic fracture

A single penny-shaped fracture of initial radius 1 m is located in the centre of a 60×90×90 m cubic region. The model is spatially discretised using 51,441 triangular and tetrahedral elements. Fracturing fluid is injected at a constant rate of Q = 0.01 m^3/s into the centre of the fracture. The Young's modulus, Poisson's ratio, viscosity and fracture toughness are set to $E = 17$ GPa, $\nu = 0.25$, μ_f = 0.0001 Pa s, and K_{ic} = 2×10^6 Pa m$^{0.5}$. This set of parameters corresponds to toughness-dominated regime, as the dimensionless viscosity defined as [45]

$$M = \mu' \left(\frac{Q^3 E'^{13}}{K'^{18} t^2} \right)^{1/5} \tag{25}$$

is less than 1 (M << 1) during the simulation time; in this equation, $\mu' = 12\mu_f$, and $K' = 4(2/\pi)^{1/2} K_{ic}$. The simulated fracture pressure, fracture aperture, and fracture radius match very well with the analytical solutions of Savitski and Detournay [45], as shown in Fig. 3. A convergence test has been also performed to investigate the robustness of the

model. For this test, three different meshes are considered: coarse (9,540 elements), medium (17,441 elements) and fine (29,080 elements). The error between injection pressures calculated from the present simulations and from the analytical solution at a time of 20s is computed and shown for different meshes in Fig. 4. The error decreases from 5% for the coarse mesh, to close to 1% for the fine mesh.

6. Simulation Results

The simulation cases are categorised into two groups, based on whether the rock matrix is permeable or not. In the impermeable cases, the effect of the fracture spacing, differential *in situ* stresses, and the position of the fracture in a series, are investigated. In cases with a permeable matrix, the effect of poroelasticity on the interaction between two fractures is investigated. Due to the simultaneous solution of the fully coupled equations, the convergence of the solution in all simulations occurs relatively fast, with three to five iterations per each timestep for an error tolerance of $\varepsilon = 1\%$.

6.1. Multiple Hydraulic Fractures in an Impermeable Rock Matrix

In these simulations, multiple parallel vertical penny-shaped fractures are considered, and the fluid is injected through a horizontal well that perforates the centre of the fractures. The size of the well is assumed to be negligible with respect to the size of the fracture, and so the wellbore is modelled as a point source boundary condition in the simulations. A total of eight cases are simulated in this section, and a summary of simulation cases is given in Table 1.

6.1.1 The effect of fracture spacing

In this case (case 1), two fractures with initial radius of 1 m are located at a distance d apart from each other. Injection rate is set to Q = 0.01 m^3/s per fracture, and the fluid viscosity is set to 0.1 Pa s. The elastic properties of the rock are set to a Young's modulus E = 20 GPa, and a Poisson's ratio ν = 0.2. An isotropic *in situ* stress is assumed, with $\sigma_x = \sigma_y = \sigma_z$ = 10 MPa. The spacing d between fractures takes on values from 5 m to 20 m. The fracture propagation paths for different spacing are shown in Fig. 5. The induced compression from the opening of the nearby fractures causes the fractures to grow away from each other. As the spacing increases, the magnitude of the induced compression felt at the growing fracture is reduced, and so the fractures tend to remain parallel to each

other. The simulation time varies between 6 to 8 hours on an Intel Xeon CPU E5-1680 v4 @ 3.40 GHz 3.40 GHz for 36,000 quadratic elements.

6.1.2 The effect of differential in situ stresses

In these simulations, three parallel vertical penny-shaped fractures of 1 m radius are considered in a 90×90×80 m cubic box. Fractures are located three metres apart from each other. The model is discretised spatially using 62,843 quadratic triangle and tetrahedral elements. A total injection rate of Q = 0.003 m^3/s is distributed among three injection points, apportioned inversely to the injection pressure of each fracture. The fluid viscosity is set to 0.1 Pa s, the elastic properties of the rock are set to Young's modulus E = 17 GPa, and Poisson's ratio ν = 0.2. The propagation increment is set to 0.5 m. Three cases are considered: one with an isotropic stress field (case 2) and two cases with anisotropic stress fields (cases 3 and 4). In case 2, all *in situ* stresses are set to 10 MPa; in case 3 it is assumed σ_x = 10, $\sigma_y = \sigma_z = 12$ MPa; and in case 4: $\sigma_x = 10$, σ_y =11, σ_z =12 MPa. The induced fractures at time $t = 20$s for cases 2 to 4 are shown in Fig. 6. As the fractures become larger than three metres in length, the interaction between fractures starts to affect their growth. The additional compressive stress from the central fracture forces the two side fractures to grow away, causing them to bend outwards. The central fracture is also under compressive stresses from the two side fractures. This excessive compression results in higher injection pressure and thus, lower injection rate in the central fracture. As these compressions are symmetric, the central fracture grows in a planar mode. In case 2, an isotropic stress field is assumed; therefore the growth of fractures is only affected by the excessive compression from the nearby fractures. But, in anisotropic cases 3 and 4, there is a competition between the differential *in situ* stresses ($\sigma_v - \sigma_h$ and $\sigma_H - \sigma_h$) and the excessive compression from the nearby fractures, to determine the direction of growth of the side fractures. The differential *in situ* stresses along the *y* and *z* directions force the side fractures to grow along the plane normal to the minimum *in situ* stress (*yz* plane). The poroelastic compression, on the other hand, pushes the side fractures to bend away from the central fracture. These opposite driving stresses result in lower curvature of the side fractures as compared to the isotropic case. In cases 3 and 4, the higher *in situ* stress acting along the *yz* plane, overcomes the excessive compression from nearby fracture, and forces the side fractures to grow in the vertical plane at some points during simulations. The central fracture continues to grow in a planar mode, due to the symmetric

compression it receives from the two side fractures. In case 3, the maximum and intermediate *in situ* stresses are equal, and so the fracture grows identically along the *y* and *z* directions.

In case 4, the higher differential *in situ* stress along the *z* direction forces the side fractures to grow vertically, while lower differential *in situ* stress along the *y* direction allows more curvature along the *y* axis. This results in the distortion of the side fractures, as shown in Fig. 6. The side fractures in the three cases described above are compared in Fig. 7 for the top and side views. The isotropic stress field produces higher curvature for side fractures, as there is no resistance from the differential *in situ* stresses. Higher differential *in situ* stresses produces lower curvature, forcing the fractures to grow vertically. The side fractures in case 4 along the *z* axis (both cases have similar vertical stress of 12 MPa) follow the same direction as in case 3, while along the *y* axis, its curvature is among those fractures in cases 2 and 3.

6.1.3 The effect of the fracture completion sequence

In these simulations, three fractures are created sequentially from a single well, each for an injection time of 102 seconds. The fractures initially have a radius of 1 m, and the growth increment is set to 0.5 m. A constant injection rate of Q = 0.001 m^3/s is assumed for each fracture, and the fluid viscosity is set to 0.1 Pa s. The elastic properties of the rock are set to E = 17 GPa, and ν = 0.2. Two cases (5 and 6) are considered: case 5 corresponds to an isotropic stress field ($\sigma_x = \sigma_y = \sigma_z$ =10 MPa), and case 6 represents the anisotropic stress field ($\sigma_x = 10$, $\sigma_y = \sigma_z$ =12 MPa). The induced fractures are shown in Figs. 8 and 9, for cases 5 and 6, respectively. The first fracture in the series grows planar, while the second and third fractures in the series grow away from the completed fracture. Again, this is due to the poroelastic compression induced by the completed fractures. The creation of the second fracture also induces compression on the completed fracture, which results in additional growth and curvature of the completed fracture. The third fracture is under even more compression from both of the previously induced fractures, and bends outward, away from the second fracture. Higher curvature is observed for the third fracture for both the isotropic and anisotropic cases. Again, the curvature of the fractures is higher for the isotropic case, as there is no resistance from the differential *in situ* stresses. As time progresses, the pressure inside the completed fractures equilibrates, and the maximum aperture of those fractures decreases. Thus, the

delay in the fracturing process may result in the pressure equilibrium within the completed fractures, and therefore, reduces their interactions. The evolution of the fluid pressures at the injection point for the three fractures is shown in Fig. 10. When injection is ceased in a fracture, the pressure dissipation within the fracture causes a drop in the pressure at the injection point. The compression induced from the subsequent fracture, on the other hand, slightly increases the pressure within the completed fracture.

6.1.4 The effect of the fracture position in a series

In these simulations, the number of fractures is increased to five, to investigate the effect of the position of each fracture within the series on the growth of each fracture. The fractures are spaced 3 m apart located in a 100×90×90 m cubic box, and injection is modelled through a single well. The model is discretised spatially using 79,133 quadratic triangle and tetrahedral elements. The total injection rate is set to Q = 0.005 m^3/s, distributed among fractures inversely proportional to their injection pressure. Two cases, 7 and 8, are assumed for simultaneous injection under isotropic ($\sigma_x = \sigma_y = \sigma_z$ =10 MPa) and anisotropic stress conditions (σ_x =10, σ_y =11, σ_z =12 MPa), respectively. The induced fractures are shown in Figure 11. The fracture in the centre continues to grow in a planar mode, due to the symmetric compression, while the other four fractures bend outward, away from the central fracture. The further the distance from the central fracture, the more curvature the fracture exhibits, due to the non-symmetric compression it receives from the other fractures. The furthest fractures on both sides show larger curvature. The second furthest fractures are under unequal compression from both sides, therefore curve less. The differential *in situ* stresses reduce fracture curvatures in anisotropic case 8. In this case, the differential *in situ* stress is pushing the fractures back to the vertical plane. The induced fractures in these two cases are compared in Fig. 12 on a horizontal cut-plane (*xy* plane) passing through the centre of the fractures. Differential *in situ* stress reduces the curvature of the fractures further.

6.2. Multiple Hydraulic Fractures in a Permeable Rock Matrix

In this section, the effect of leakoff and poroelasticity on the interactions between two fractures is investigated. Two parallel fractures are placed 5 m apart. The injection is performed simultaneously at a rate of Q = 0.01 m^3/s, with a fluid with viscosity of 0.0001 Pa s. The elastic properties of the rock are set to E = 20 GPa, and ν = 0.2, and fracture

toughness is set to K_{ic} = 2×10^6 Pa m$^{0.5}$. With these parameters, the hydraulic fracturing process falls under the toughness-dominated regime. An isotropic *in situ* stress is assumed, with σ = 10 MPa.

The leakoff is allowed by introducing matrix permeability. Several cases are simulated in which the matrix permeability (k_m) varies between 1×10^{-16}, and 1×10^{-15} m^2, and the Biot coefficient (α) also varies between 0, 0.5 and 1. The permeability of 1×10^{-15} m^2 corresponds to the leakoff-toughness regime [7]. The curvature of one of the fractures is shown in Fig. 13, where it is compared with the results for an impermeable matrix for both toughness- and viscosity-dominated cases. Interesting remarks can be concluded from the results shown in Fig. 13.

(a) In the absence of poroelastic effects ($\alpha = 0$), the matrix permeability does not affect the curvature of the fracture. Higher permeability increases the leakoff and it takes longer injection time and higher volume of the fluid to create the fracture; however, due to the uncoupled flow-deformation in the matrix, the interaction between fractures remains purely mechanical and a consequence of the fracture aperture opening.

(b) In lower matrix permeability, the leakoff and poroelastic interactions between fractures has minimal effect on the propagation direction.

(c) In leakoff-dominated cases, poroelastic effects are significant and affect the propagation direction of two interacting fractures. Additional compression from the expanded matrix pushes the fractures to propagate away from each other and that increases the curvature of the induced fracture.

(d) The effects of poroelasticity increases with increasing Biot coefficient. This can be seen in both low and high permeability cases.

(e) The fractures in toughness regime have lower interactions than those in viscosity regime. This can be explained by lower fracture aperture in fractures under toughness regime [7].

7. Conclusions

A fully coupled three-dimensional finite element model has been presented for the simulation of the growth of multiple hydraulic fractures in permeable rocks. The model was validated against various analytical solutions and experimental data, including plane-strain and penny-shaped fractures in different regimes of propagation. Several cases of simultaneous and sequential fracturing are simulated. Results show that the compression

induced from the nearby fractures, and by the differential *in situ* stresses, have opposite effects on the growth of the hydraulic fractures. The fractures tend to grow away from each other due to the effect of nearby fractures, whereas the differential *in situ* stresses force the fracture to grow in a plane perpendicular to the minimum *in situ* stress. The interaction between two nearby fractures reduces by increasing spacing. The competition between the compressive stresses due to fracture interactions, and the *in situ* differential stresses, dictates the shape of the hydraulic fracture. Non-identical differential *in situ* stresses i.e. $\sigma_z - \sigma_x \neq \sigma_y - \sigma_x$, causes distortion in the fracture shape along the *y* and *z* directions. The fractures in a series of hydraulic fractures, induced simultaneously from a single well, may have different curvatures, due to non-symmetric compression they receive from the nearby fractures. Fractures located closer to the centre of the series are expected to grow straight, while fractures located close to the end of the series may show higher curvature. In sequential fracturing, the completed fractures may also affect the new induced fractures and make them bend outward, away from the completed fractures. Poroelastic effects can be significant when the leakoff is significant, *i.e.*, when fractures are propagating in the leakoff-dominated regime. Without poroelastic coupling, the matrix permeability has no effect on the interactions between two fractures, and the fractures propagate in the same direction as in the no-leakoff case.

Acknowledgments

The authors thank Engineering and Physical Sciences Research Council (EPSRC) for supporting this work, through the CONTAIN Project EP/K036025/1. They also thank the European Commission for partially funding this work through the TRUST Collaborative Project, 309067.

References

[1] Economides MJ, Nolte KG, eds. 2000. *Reservoir Stimulation*. New York: Wiley. 3rd ed.

[2] Adachi J, Siebrits E, Peirce A, Desroches J. Computer simulation of hydraulic fractures. Int. J. Rock Mech. Min. Sci. 2007; 44: 739–757.

[3] Waters GA, Barry KD, et al. Simultaneous hydraulic fracturing of adjacent horizontal wells in Woodford shale. SPE Hydraulic Fracturing Technology Conference, Woodlands, Texas, Jan. 19-21, 2009, paper SPE 119635-MS.

[4] Peirce AP, Siebrits E. Uniform asymptotic approximations for accurate modeling of cracks in layered elastic media. Int. J. Fract. 2001: 110: 205–239.

[5] Marina S, Imo-Imo EK, Ingham D, Mohamed P, Yong S. Modelling of hydraulic fracturing process by coupled discrete element and fluid dynamic methods. Environ. Earth Sci. 2014; 72: 3383–3399.

[6] Carrier B, Granet S. Numerical modelling of hydraulic fracture problem in permeable medium using cohesive zone model. Eng. Fract. Mech. 2012; 79: 312-328.

[7] Salimzadeh S, Paluszny A, Zimmerman RW. Three-dimensional poroelastic effects during hydraulic fracturing in permeable rocks. Int. J. Solids Struct. 2016; 108: 153-163.

[8] Salimzadeh S, Paluszny A, Zimmerman RW. Thermal Effects during Hydraulic Fracturing in Low-Permeability Brittle Rocks, in Proceeding of the 50th US Rock Mechanics Symposium, Houston, Texas, 26-29 June 2016, paper ARMA 16-368.

[9] Fu P, Johnson SM, Carrigan CR. An explicitly coupled hydro-geomechanical model for simulating hydraulic fracturing in arbitrary discrete fracture networks. Int. J. Numer. Anal. Meth. Geomech. 2013; 37: 2278-2300.

[10] Norbeck JH, McClure MW, Lo WJ, Horne RN. An embedded fracture modeling framework for simulation of hydraulic fracturing and shear stimulation. Comput. Geosci. 2016; 20: 1-18.

[11] Grassl P, Fahy C, Gallipoli D, Wheeler SJ. On a 2D hydro-mechanical lattice approach for modelling hydraulic fracture. J. Mech. Phys. Solids 2015; 75: 104-118.

[12] Chukwudozie CP. Application of the variational fracture model to hydraulic fracturing in poroelastic media. PhD dissertation, Louisiana State University, 2016.

[13] Dahi-Taleghani A. Analysis of hydraulic fracture propagation in fractured reservoirs: an improved model for the interaction between induced and natural fractures. PhD dissertation, University of Texas at Austin, 2009.

[14] Salimzadeh S, Khalili N. A three-phase XFEM model for hydraulic fracturing with cohesive crack propagation. Comput. Geotechnics 2015; 69: 82-92.

[15] Salimzadeh S, Khalili N. A fully coupled XFEM model for flow and deformation in fractured porous media with explicit fracture flow. Int. J. Geomech. 2016: 16: 04015091.

[16] Batchelor GK. An Introduction to Fluid Dynamics. Cambridge: Cambridge University Press; 1967.

[17] Zimmerman RW, Bodvarsson GS. Hydraulic conductivity of rock fractures. Transp. Porous Media 1996; 23: 1–30.

[18] Geertsma J, de Klerk F. A rapid method of predicting width and extent of hydraulically induced fractures. J. Petrol. Tech. 1969; 21: 1571–1581.

[19] Spence DA, Sharp P. Self-similar solutions for elastohydrodynamic cavity flow. Proc. Royal Soc. London A 1985; 400: 289-313.

[20] Fisher M, Heinze J, Harris C, et al. Optimizing horizontal completion techniques in the Barnett Shale using microseismic fracture mapping. In: Proceedings of the Annual Technical Conference and Exhibition, Houston, 26-29 September 2004. Paper SPE-90051-MS.

[21] Olson JE, Taleghani AD. Modeling simultaneous growth of multiple hydraulic fractures and their interaction with natural fractures. In: Proceedings of the SPE Hydraulic Fracturing Technology Conference, The Woodlands, Texas, 19-21 January 2009. Paper SPE-119739-MS.

[22] Cheng Y. Boundary element analysis of the stress distribution around multiple fractures: implications for the spacing of perforation clusters of hydraulically fractured horizontal

wells. In: Proceedings of the SPE Eastern Regional Meeting, Charleston, West Virginia, 23-25 September 2009. Paper SPE-125769-MS.

[23] Rafiee M, Soliman MY, et al. Geomechanical considerations in hydraulic fracturing designs. In: Proceedings of the SPE Canadian Unconventional Resources Conference, Calgary, 2012. Paper SPE-162637-MS.

[24] Bunger AP, Zhang X, Jeffrey RG. Parameters affecting the interaction among closely spaced hydraulic fractures. SPE J. 2012; 17: 292-306.

[25] Kresse O, Weng X, Gu H, Wu R. Numerical modeling of hydraulic fracture interaction in complex naturally fractures formations. Rock Mech. Rock Eng. 2013; 46(3): 555-568.

[26] Wong SW, Geilikman M, Xu G. The geomechanical interaction of multiple hydraulic fractures in horizontal wells. In: Effective and Sustainable Hydraulic Fracturing, R Jeffrey (Ed.), InTech Publishers, 2013.

[27] Gupta P, Duarte CA. Simulation of non-planar three-dimensional hydraulic fracture propagation. Int. J. Numer. Anal. Meth. Geomech. 2014; 38: 1397-1430.

[28] Sesetty V, Ghassemi A. Simulation of simultaneous and zipper fractures in shale formations. In: Proceedings 49th US Rock Mechanics Symposium, San Francisco, 2015, paper ARMA 2015-558.

[29] Peirce A, Bunger A. Interference fracturing: Nonuniform distributions of perforation clusters that promote simultaneous growth of multiple hydraulic fractures. SPE J. 2015; 20: 384-395.

[30] Kumar D, Ghassemi A. 3D simulation of multiple fracture propagation from horizontal wells. In: Proceedings 49th US Rock Mechanics Symposium, San Francisco, paper ARMA 2015-585.

[31] Safari R, Lewis R, Ma X, Multu U, Ghassemi A. Infill-well fracturing optimisation in tightly spaced horizontal wells. SPE J. 2015; 22: 582-595.

[32] Settgast RR, Fu P, Walsh SDC, et al. 2016. A fully coupled method for massively parallel simulation of hydraulically driven fractures in 3-dimensions. Int. J. Numer. Anal. Meth. Geomech. 2016; 41: 627-653.

[33] Usui T, Salimzadeh S, Paluszny A, Zimmerman RW. Effect of poroelasticity on hydraulic fracture interactions. In: Proceedings of the 6th Biot Conference on Poromechanics, Paris, France, 9-13 July 2017.

[34] Paluszny A, Zimmerman RW. Numerical fracture growth modeling using smooth surface geometric deformation. Eng. Fract. Mech. 2013; 108: 19–36.

[35] Kuna M. Finite elements in fracture mechanics: theory – numerics – applications. Dordrecht: Springer; 2013.

[36] Detournay E. Propagation regimes of fluid-driven fractures in impermeable rocks. Int. J. Geomech. 2004; 4: 1–11.

[37] Witherspoon PA, Wang JSY, Iwai K, Gale JE. Validity of cubic law for fluid flow in a deformable rock fracture. Water Resourc. Res. 1980: 16: 1016–1024.

[38] Biot MA. A general theory of three dimensional consolidation. J. Appl. Phys. 1941: 12: 155–164.

[39] Zimmerman RW. Coupling in poroelasticity and thermoelasticity. Int. J. Rock Mech. Min. Sci. 2000; 37: 79-87.

[40] Paluszny A, Zimmerman RW. Numerical simulation of multiple 3D fracture propagation using arbitrary meshes. Comput. Meth. Appl. Mech. Eng. 2011; 200: 953-966.

[41] Matthäi SK, Geiger S, Roberts SG. The complex systems platform csp3.0: Users guide, Technical report, ETH Zürich Research Reports, 2001.

[42] Stüben K. A review of algebraic multigrid. J. Comput. Appl. Math. 2001; 128: 281-309.

[43] Schöllmann M, Richard HA, Kullmer G, Fulland M. A new criterion for the prediction of crack development in multiaxially loaded structures. Int. J. Fract. 2002; 117: 129–41.

[44] Khristianovic SA, Zheltov YP. Formation of vertical fractures by means of highly viscous liquid. In: Proceedings of the 4th World Petroleum Congress, Rome, 1955, pp. 579–86.

[45] Savitski A, Detournay E. Propagation of a penny-shaped fluid-driven fracture in an impermeable rock: asymptotic solutions. *Int. J. Solids Struct.* 2002; 39(26): 6311–6337.

Table 1- Material properties of the simulation cases in impermeable matrix

Case No.	Description	*In situ* Stress σ_x (MPa)	*In situ* Stress σ_y (MPa)	*In situ* Stress σ_z (MPa)	Young's Modulus (GPa)	Poisson's Ratio
1	Simultaneous – 2 Fractures	10	10	10	20	0.2
2	Simultaneous – 3 Fractures	10	10	10	17	0.2
3	Simultaneous – 3 Fractures	10	12	12	17	0.2
4	Simultaneous – 3 Fractures	10	11	12	17	0.2
5	Sequential – 3 Fractures	10	10	10	17	0.2
6	Sequential – 3 Fractures	10	12	12	17	0.2
7	Simultaneous – 5 Fractures	10	10	10	17	0.2
8	Simultaneous – 5 Fractures	10	11	12	17	0.2

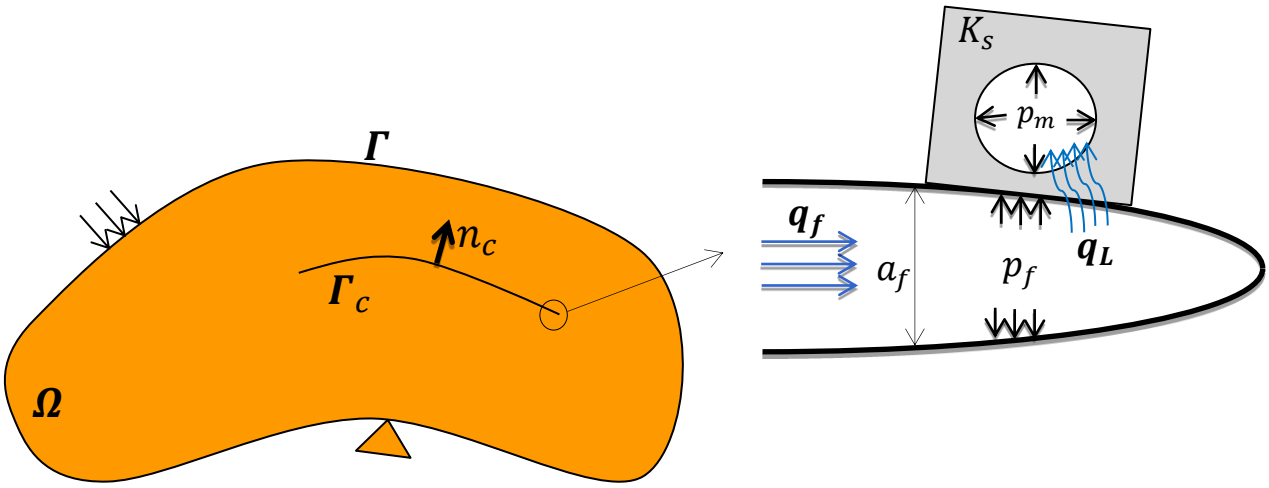

Figure 1. Schematic representation of the problem with discrete fracture, a_f is the fracture aperture, p_f is the fluid pressure in the fracture, p_m is the fluid pressure in the matrix, q_f is flow rate in the fracture, q_L is the leakoff, and K_s is the bulk modulus of the solid grains.

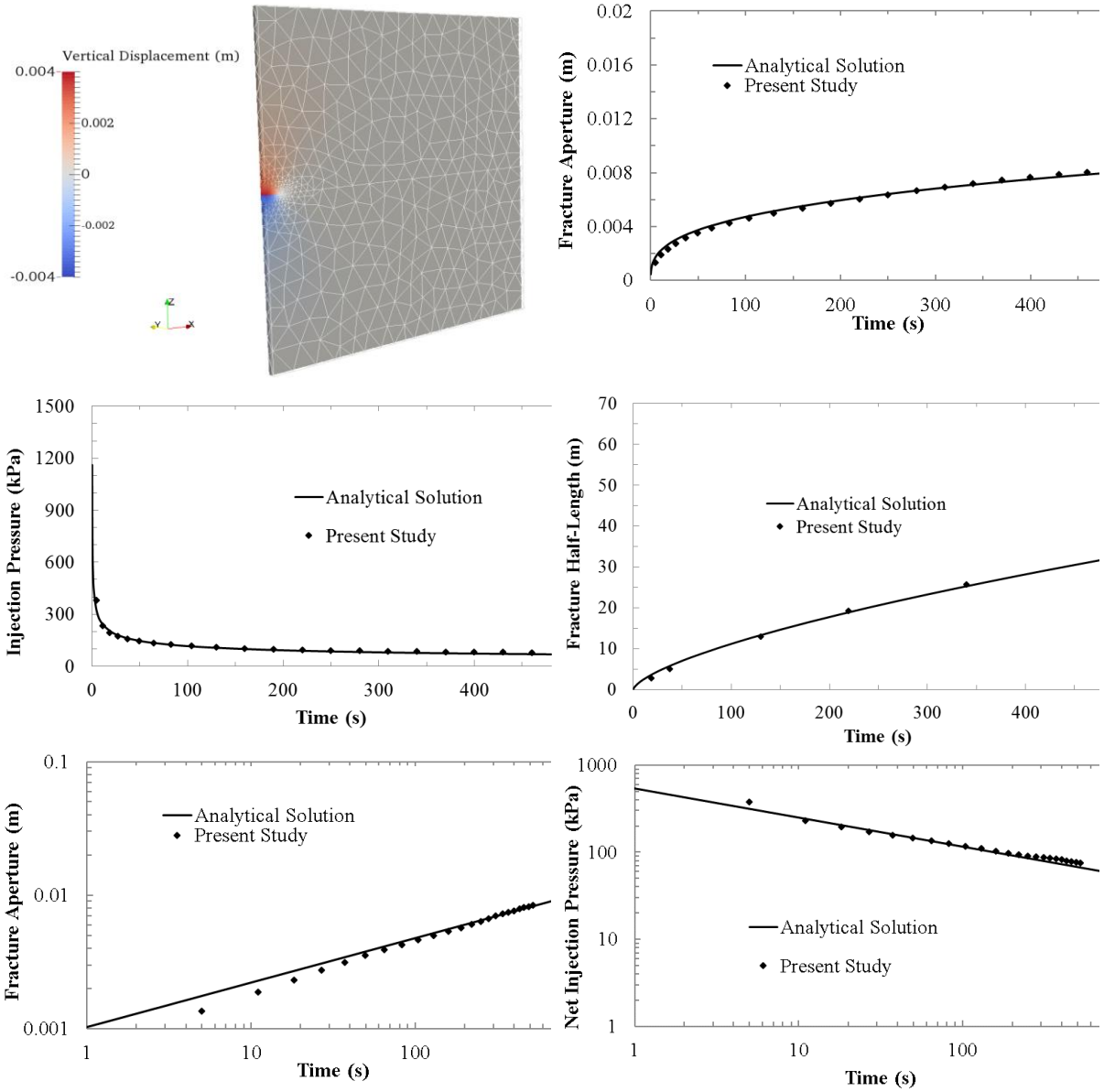

Figure 2. Validation example: plane-strain hydraulic fracture (KGD fracture). Analytical solution is given by Geertsma and de Klerk [18]

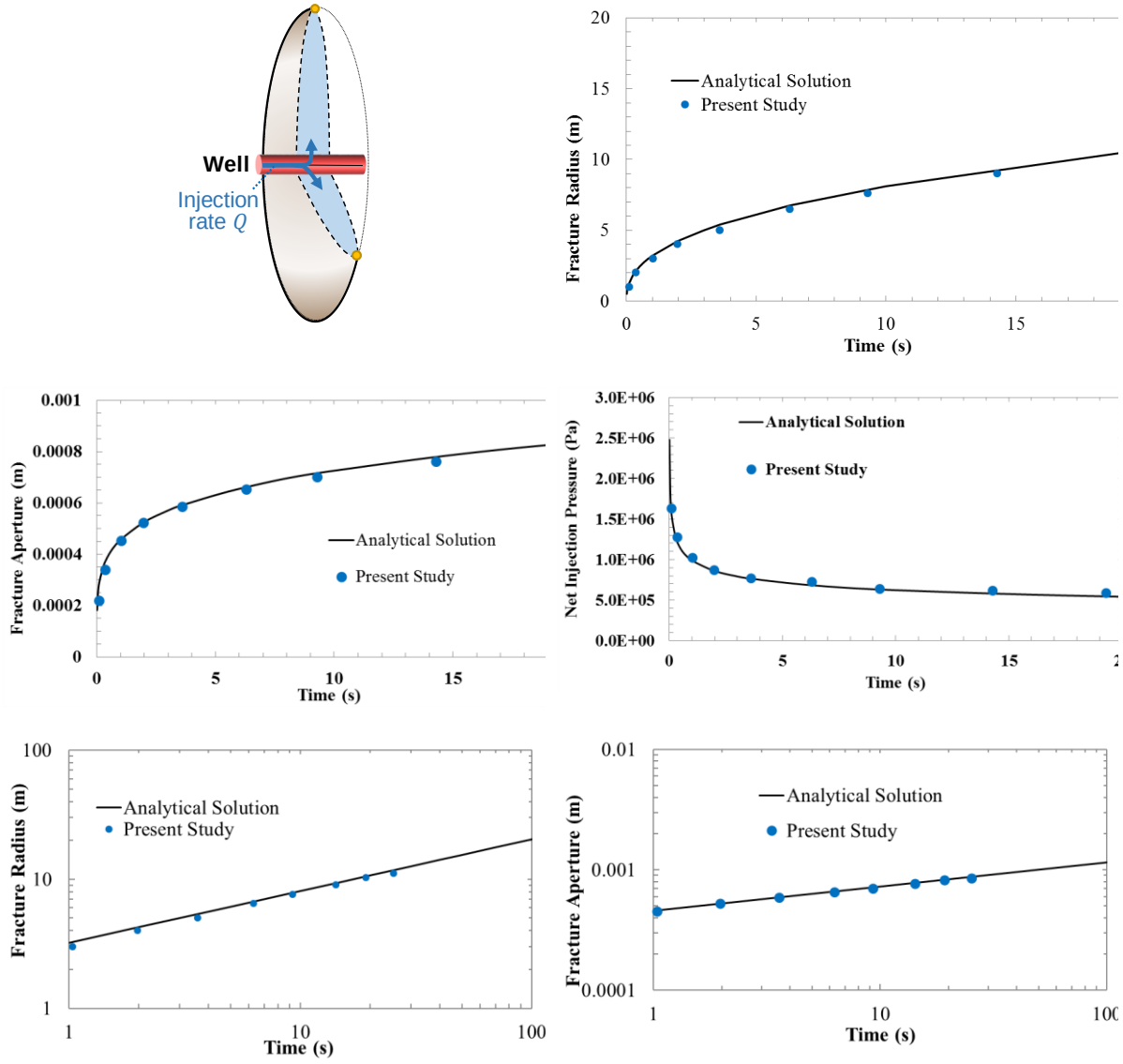

Figure 3. Validation example: penny-shaped hydraulic fracture (radial fracture). Analytical solution is given by Savitski and Detournay [46]

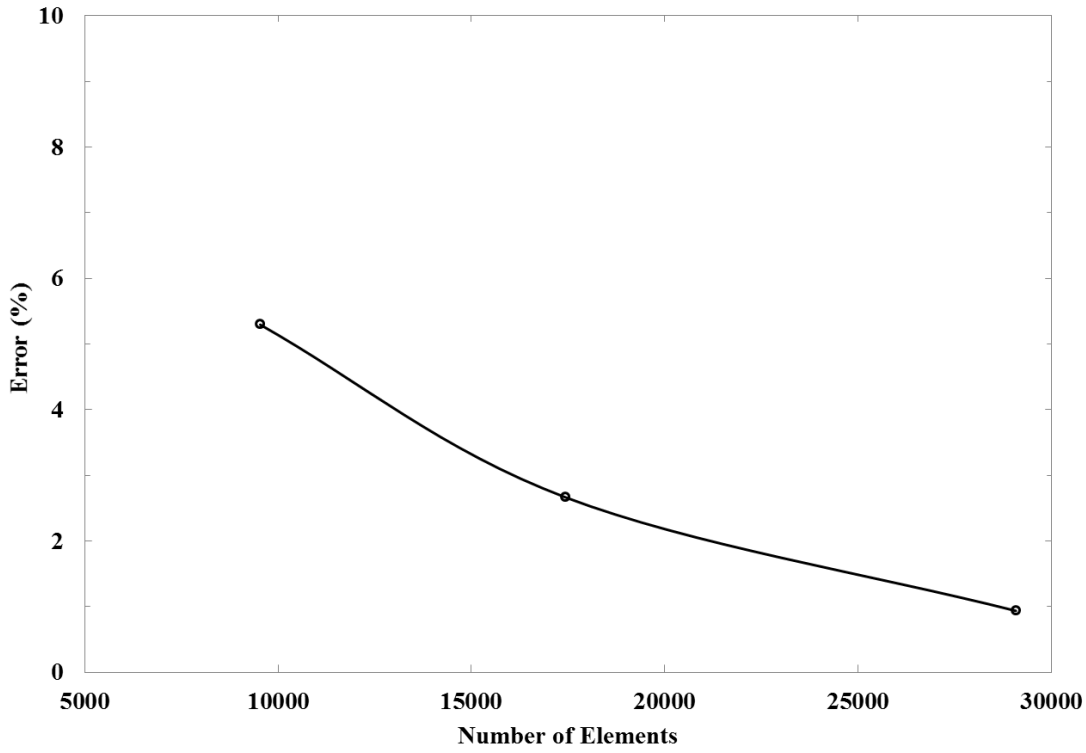

Figure 4. Convergence test for the penny-shaped fracture with three different meshes. Error is calculated for injection pressure at time of 20s.

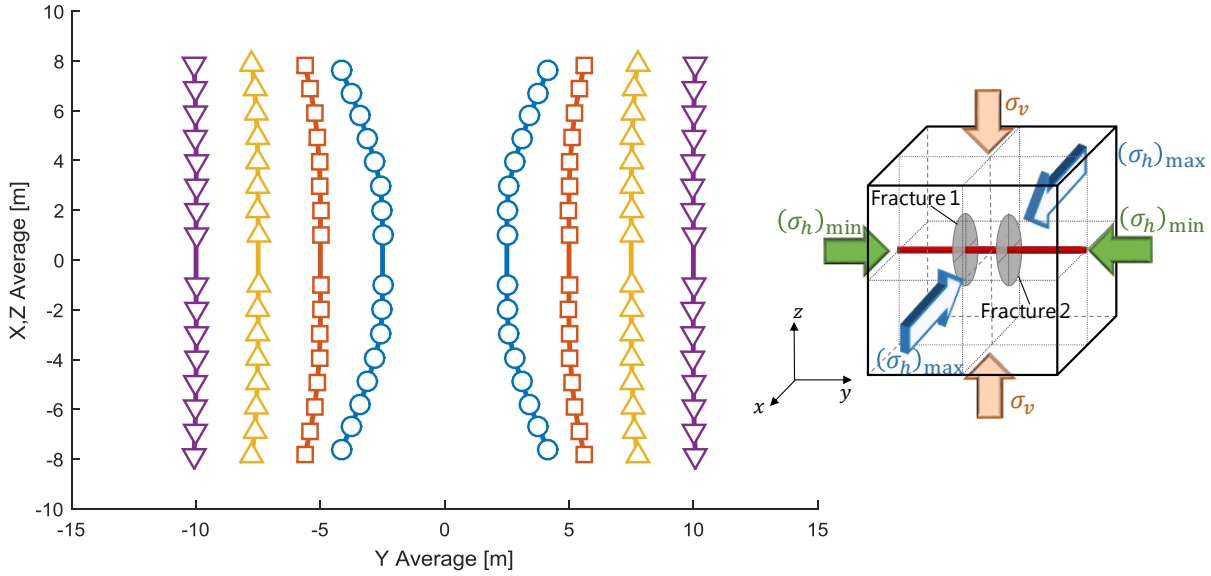

Figure 5. The effect of the spacing between fractures on the propagation paths of the fractures

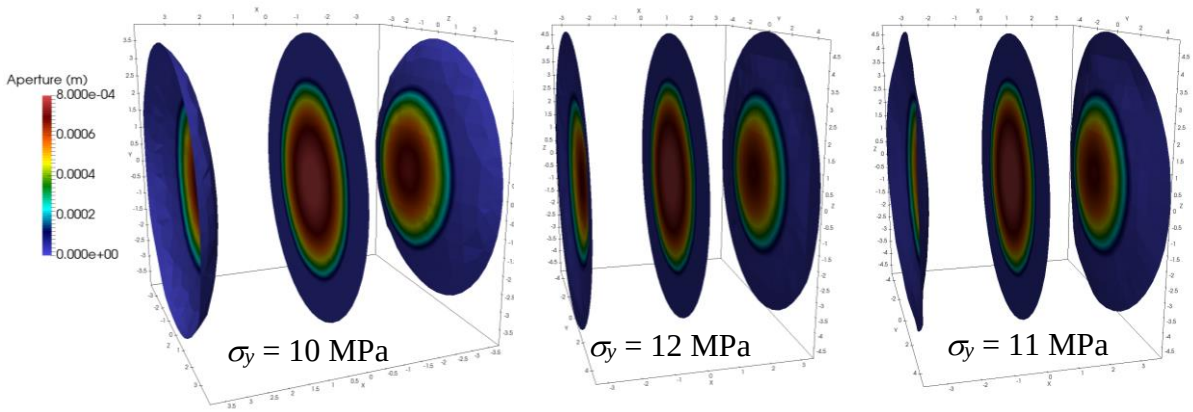

Figure 6. Simultaneous injection of three hydraulic fractures under isotropic and anisotropic stress fields (cases 2 to 4)

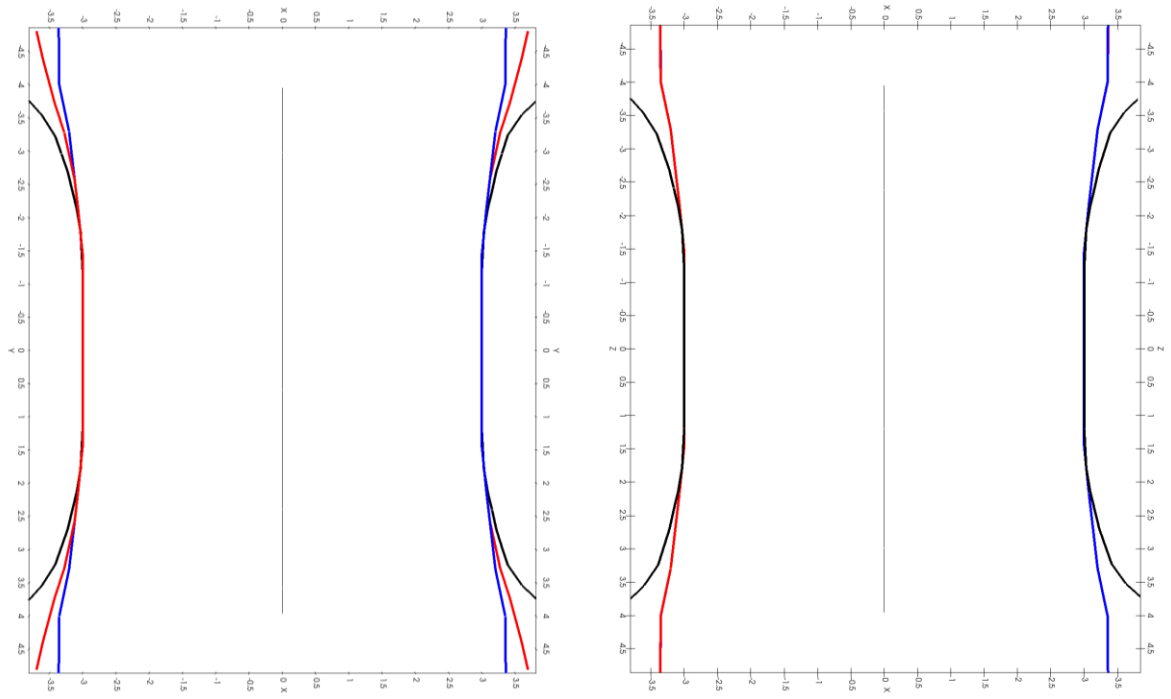

Vertical Cut Plane
y = 0

Horizontal Cut Plane
z = 0

Figure 7. Comparison between the direction of growth of hydraulic fractures under different stress field: case 2 (black), 3 (blue) and 4 (red), in simultaneous injection (side and top views)

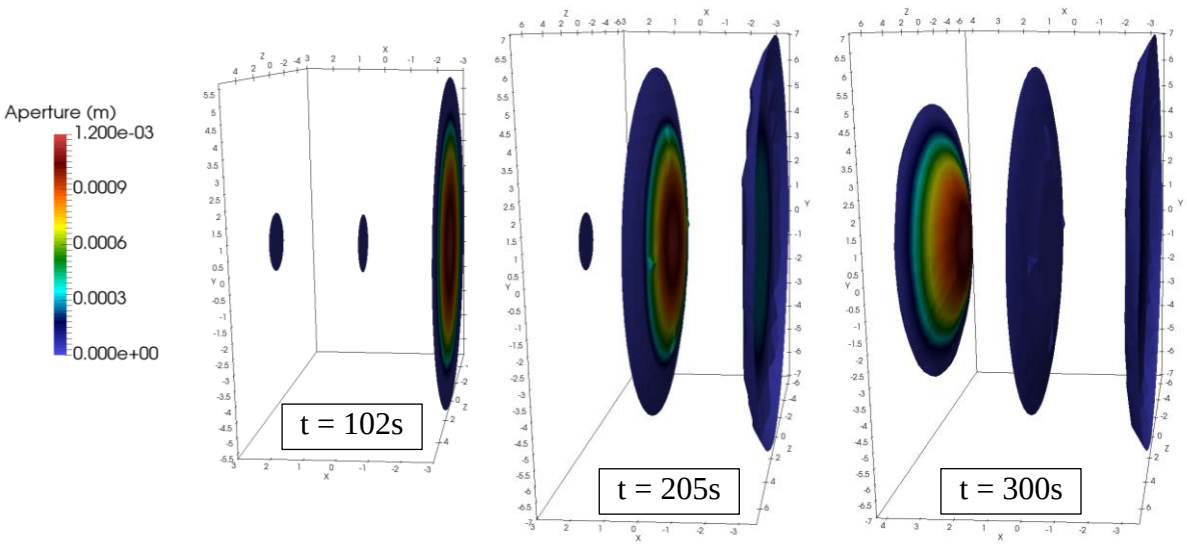

Figure 8. Sequential injection of three hydraulic fractures under isotropic stress field (case 5)

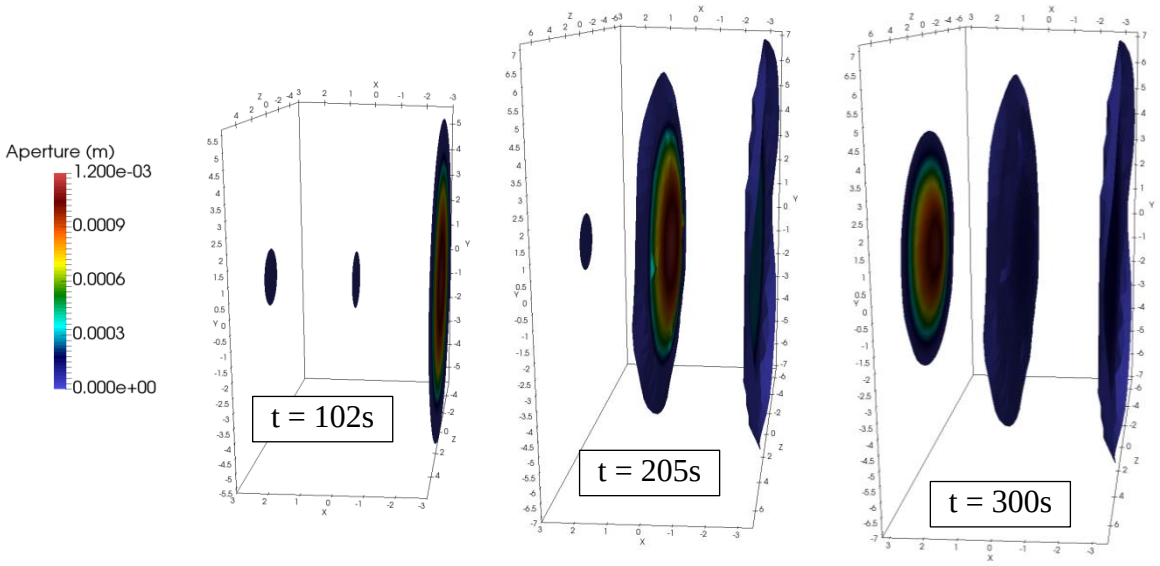

Figure 9. Sequential injection of three hydraulic fractures under anisotropic stress field (case 6)

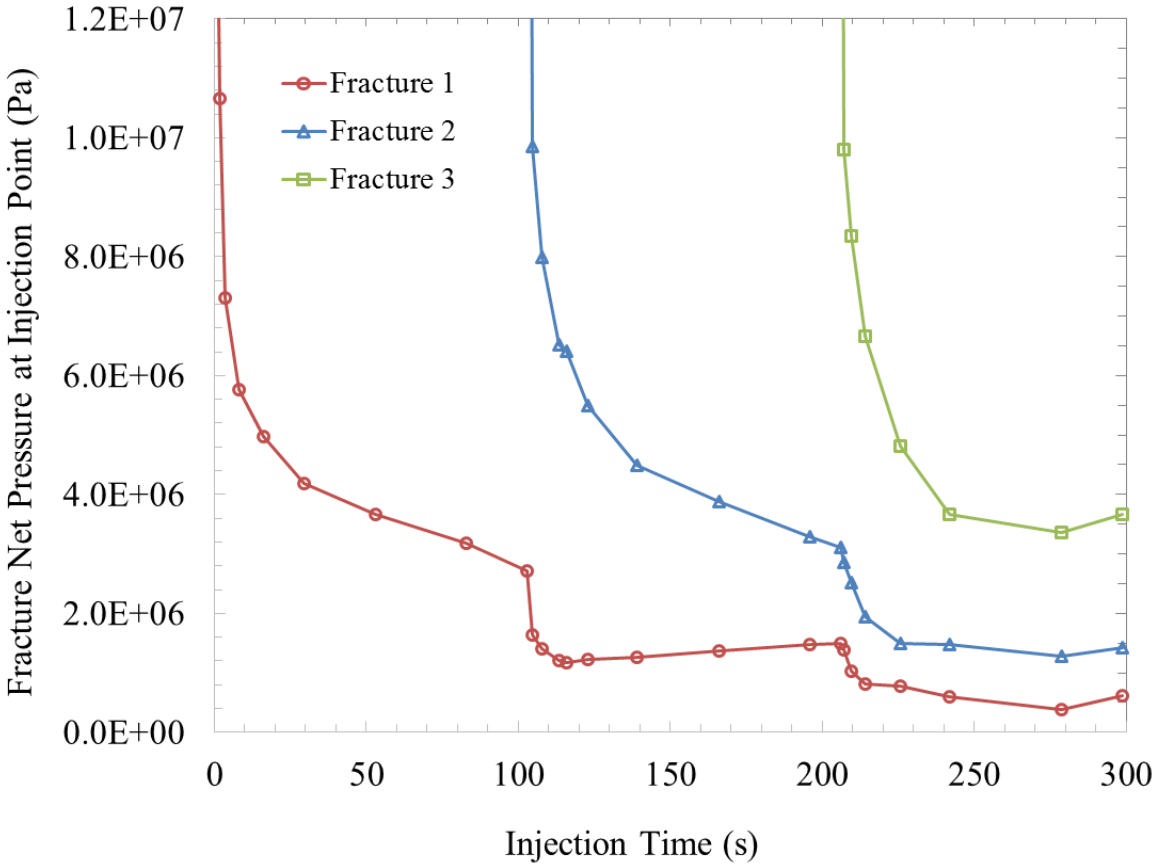

Figure 10. Fracture net pressure at injection point versus time for different fractures in sequential fracturing

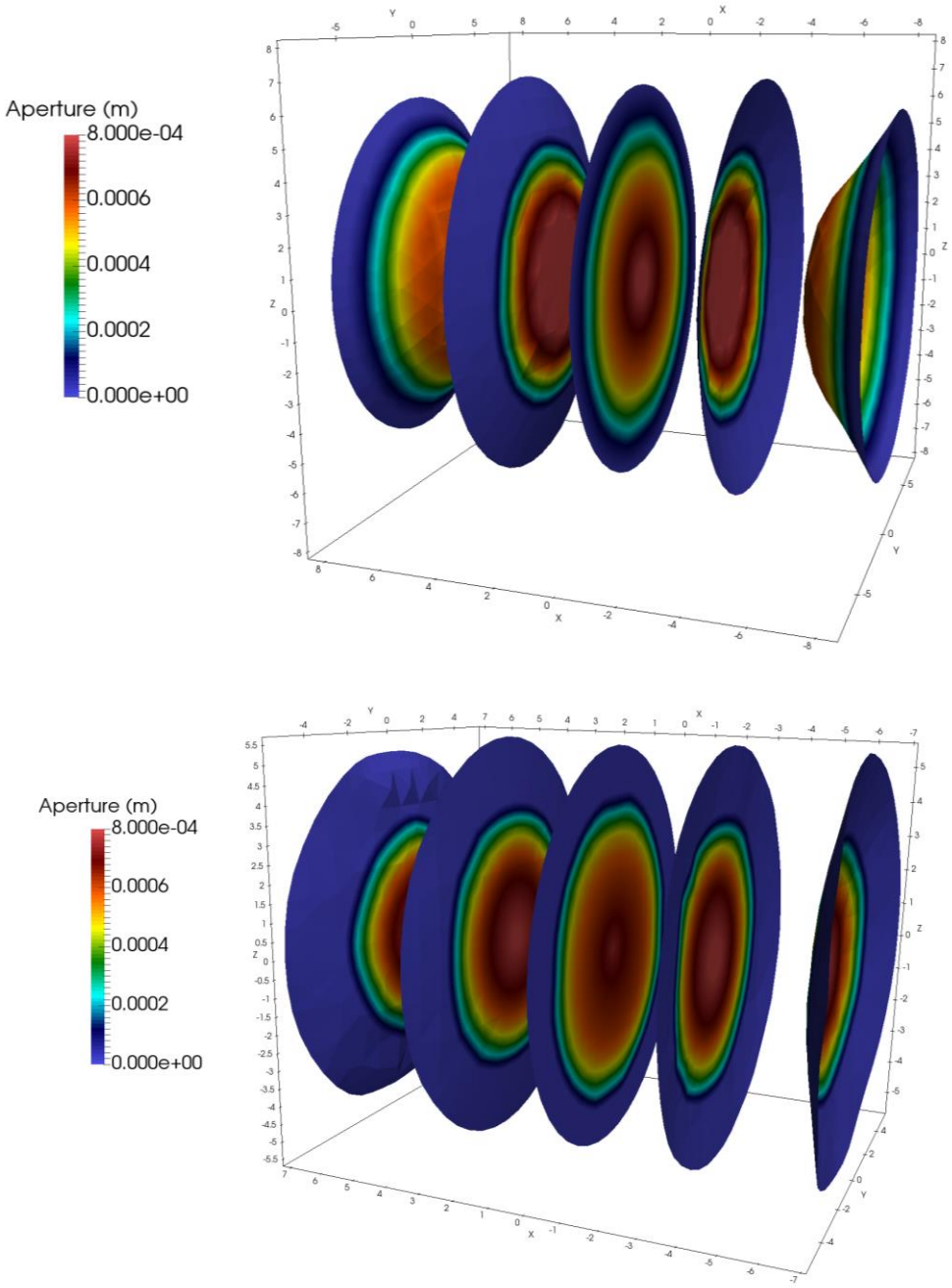

Figure 11. Simultaneous injection of five hydraulic fractures under isotropic (a) and anisotropic (b) stress field (cases 7 and 8)

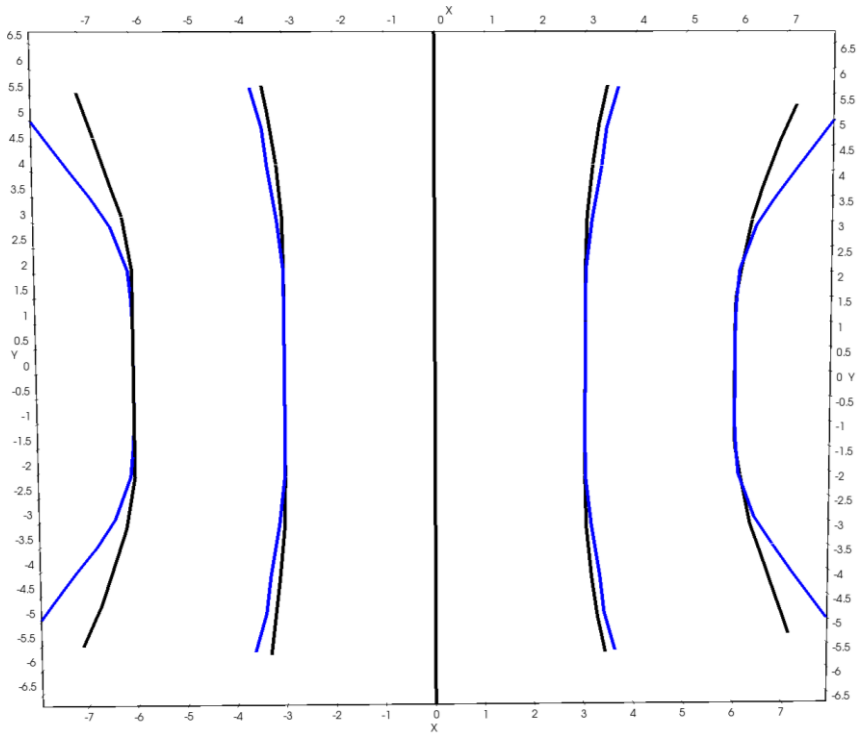

Figure 12. Comparison between the direction of growth of five hydraulic fractures under isotropic and anisotropic stress fields (cases 7 and 8), in simultaneous injection (top view). Blue lines represent the isotropic stress field (case 7), and black lines show anisotropic stress field (case 8)

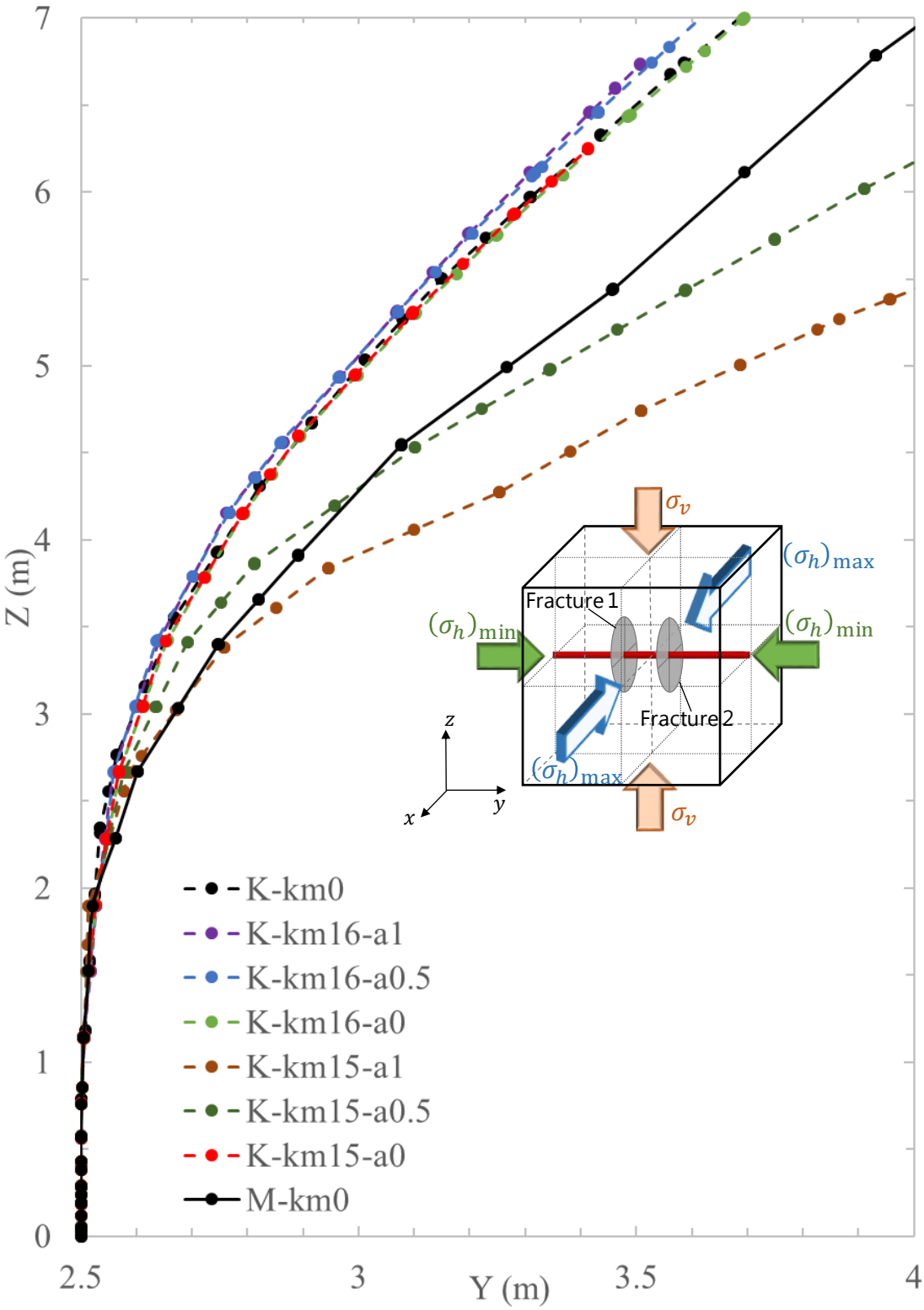

Figure 13. The effect of leakoff on the curvature of a fracture: matrix permeability (k_m) varies between 0, 1×10^{-16}, and 1×10^{-15} m^2; and Biot coefficient (α) varies between 0, 0.5 and 1